Sol-gel coatings doped with graphene nanoplatelets for improving the degradation rate and the cytocompatibility of AZ31 alloy for biomedical applications

*J.P. Fernández-Hernán [1, *], B. Torres [1], A.J. López [1], E. Martínez-Campos [2], J. Rams[1].*

[1] Área de Ciencia e Ingeniería de Materiales, ESCET, Universidad Rey Juan Carlos,

C/Tulipán s/n 28933, Móstoles, España.

[2] Instituto de Estudios Biofuncionales, ICTP-CSIC, Universidad Complutense de Madrid,

Paseo Juan XXIII nº 1, 28045, Madrid, España.

ABSTRACT

SiO_2 coatings doped with four different functionalized graphene nanoplatelets (COOH-GNPs) concentrations (from 0.005 to 1 wt.%) were deposited on AZ31 magnesium substrates to control the corrosion rate and to increase the cytocompatibility of this alloy for MC3T3 pre-osteoblastic cells, to develop biodegradable implants for bone fracture and orthopedic applications. The results show that the highest nanoplatelets concentration promoted the generation of nanoparticle aggregates acting as crack-nucleation points embedded in the coating, decreasing the protective behavior of these coatings. Nanoplatelets concentrations of 0.005 wt.% and 0.05 wt.% led to obtaining crack-free coatings that provided an improved barrier effect. Cytocompatibility tests show that all the conditions, even the bare AZ31, led to cell proliferation. However, low cell adhesion was found in the bare substrate, contrary to the coated substrates. The coatings with the highest nanoplates concentrations augmented the metabolic activity of cell cultures. The sol-gel coating doped with 0.05 wt.% COOH-GNPs presented the best corrosion rate control behavior and improved cytocompatibility, with the generation of a confluent preosteoblastic monolayer on its surface after one week of cell culture.

* Corresponding author: Juan Pablo Fernández Hernán
  juanpablo.fernandez@urjc.es
+34 646204239, +34 914888252
C/ Tulipán s/n, 28933, Departamental I - 009.2, Móstoles (Spain)

1.   **Introduction**

The use of magnesium alloys for the manufacture of temporary implants for the treatment of bone fractures is very attractive due to their outstanding properties [1 – 5]. It is well known that magnesium is a biocompatible metal that, once implanted in a biological environment, degrades until its total disappearance. Magnesium alloys present an elastic modulus and density values lower than those of other metals and alloys often used in implantology like surgical 316L stainless steel, Ti6Al4V, and Cr-Co. Moreover, magnesium presents elastic modulus and density values closer to those of the cortical bone tissue. Thus, the use of magnesium alloys for bone fracture treatments can positively affect the healing process, avoiding the prevalence of adverse effects such as the stress-shielding effect [6, 7], that could increase the healing time or even cause the failure of the implant, requiring a new surgery to remove the implant.

In addition to the mechanical properties, Mg^{2+} cation, which is generated during the oxidation process of magnesium in aqueous solutions (equation 1), is a fundamental element present in different physiological processes that take place in the organism. Magnesium is known for being involved in the bone tissue generation process and, therefore, it can promote the growth of bone tissue [8, 9]. Thus, at a physiological level, its presence can improve the interaction between osteoblasts, *i.e*., cells in charge of generating new bone tissue, and the surface of the implant, increasing the osseointegration and the success rate of the medical treatments.

$$Mg + H_2O \rightarrow Mg^{+2} + 2OH^- + H_2 \tag{1}$$
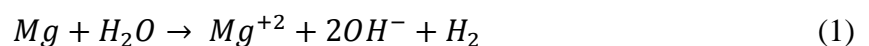
Despite all of these extraordinary properties that magnesium and its alloys present for the manufacture of temporary implants, their use is not widespread in the implantology industry due to their main drawback; magnesium is a very reactive metal, prone to suffer corrosion with

a high degradation rate. Moreover, during the corrosion process of magnesium H_2 is generated. Therefore, these alloys present two different problems derived from the high reactivity of magnesium. The first problem is related to the high degradation rate. Thus, loss of mechanical integrity of the implant may occur prior to complete bone healing, causing the failure of the treatment. The second problem is related to the hydrogen evolution as a by-product of the corrosion reaction of magnesium (equation 1). If the hydrogen evolution rate is greater than that the capacity of the organism to eliminate it, hydrogen will accumulate around the implant making changes in pH and other physiological conditions that could affect the homeostasis, leading to medical problems. Moreover, a high rate of hydrogen evolution on the surface of the implant could difficult the dispersion and adhesion of bone cells, decreasing the osseointegration of the implant, with the subsequent healing problems.

Therefore, the main challenge is to control the degradation rate of these alloys to make them more suitable for the development of temporary implants. Among the different strategies that can be followed to achieve this, the use of coatings can be a feasible solution to temporarily isolate the implant from the aggressive outer medium that degrades it, delaying and decreasing the degradation of the implant and reducing the generation rate of H_2 to a level where it can be assimilated by the organism without any adverse response.

For coating generation, the sol-gel synthesis process combined with a coating method like dip-coating is a low-cost and environmentally friendly process that has shown its versatility and utility to generate thin, compact, and defect-free coatings that perform good protection against corrosion and help to control the degradation rate of magnesium alloys [10 – 12]. The sol-gel coatings deposited on magnesium alloys show good adhesion to the grounded surface of the substrates. In previous research [13], these coatings presented shear stress resistance up to 15 MPa, in the case of substrates grounded with 1200 SiC grit papers, and up to 23 MPa for substrates grounded with 400 SiC grit paper. Moreover, one of the most powerful features of the sol-gel method is that during the synthesis process, different molecules and particles like

growth factors, corrosion inhibitors, or antibiotics, among a wide range of possibilities, can be easily added to the solution to provide new properties to the final coatings [14 – 20]. Finally, this method allows generating layer-structured or multifunctional coatings by generating several layers that provide different properties to the final coating [21 – 23].

The use of silicon alkoxides as precursor molecules for the generation of silica sol-gel coatings is present in the scientific literature [24 – 26]. When a coating is intended to be developed for a biocompatible purpose, more specifically to be in contact with bone tissue, the use of silicon-based materials for the generation of the coating that will be in contact with the bone cells can increase the biocompatibility and the osseointegration of those coatings, because silicon is known for being an important element for the mineralization and generation of bone tissue, due to its effect for enhancing the osteoblastic cell activity [27 – 29].

Since its discovery in 2004 by Geim and Novoselov, graphene has aroused great interest due to its outstanding properties and possibilities to be applied in different fields. The use of graphene nanoplatelets as filler particles to improve corrosion protection properties of coatings was reported in the scientific literature by several authors [30 – 34]. The addition of graphene as nanoreinforcement improves corrosion protection by acting as an obstacle for the aggressive molecules of the medium in their way to reach the surface of the metallic substrate. Moreover, the addition of graphene can provide mechanical stability, avoiding the generation of defects in the coatings and, therefore, increasing their protective behavior.

Regarding biocompatibility, different authors have reported the cytocompatibility of graphene-based materials embedded in polymer matrixes. D. Depan et al. [35] found that the incorporation of COOH-functionalized graphene nanoplatelets into chitosan scaffolds significantly enhanced the adhesion, proliferation, and growth of the MC3T3-E1 mouse pre-osteoblast cell line cultures. Different physicochemical factors like modified roughness at a nanometric scale and increased surface area, as well as the hydrophilic nature of the COOH-functionalized nanoparticles, were related to the cytocompatibility enhancement. A. Aryaei et

al. [36] used the chemical vapor deposition (CVD) method to generate a layer of graphene on different substrates made out of SiO_2, soda-lime glass, and stainless steel. They assessed their interaction with osteoblastic cells and concluded that graphene did not have any cytotoxic effect on the osteoblasts. Furthermore, the graphene layer influenced the cell attachment in the case of the SiO_2 and stainless-steel substrates, where the cellular adhesion was significantly increased when compared with the substrates without the graphene layer.

The objective of the present research is to establish a method to improve the osseointegration of this interesting magnesium alloy for the manufacture of biodegradable implants. Assessing the corrosion protection and the *in vitro* cytocompatibility of AZ31 magnesium alloy substrates coated with ceramic SiO_2 coatings doped with different proportions of functionalized graphene nanoplatelets. Moreover, the optimal COOH-GNPs concentration was investigated, to provide the best balance between corrosion protection and cytocompatibility for pre-osteoblastic cells.

2. Materials and methods

2.1 Magnesium Alloy

AZ31 magnesium plates used in this research were provided by Magnesium Elektron. The composition of the alloy is shown in table I. From these plates, samples of 1.5×1.5 cm^2 were cut and then polished to 1200 grain size with SiC grit papers. Finally, previous to the coating process, the samples were immersed in an ultrasonic bath of isopropanol for 10 minutes, to clean and degrease their surface, and then dried with hot air.

Table I. Composition of the AZ31 Mg alloy.

Al	Zn	Mn	Si	Ca	Fe	Ni	Cu	Mg
2.9	0.75	0.29	0.01	<0.005	0.04	0.0013	<0.0005	Balance

2.2 Coating generation

In this research, five different SiO$_2$ monolayer coatings were generated through the sol-gel synthesis process in combination with the dip-coating method. Tetraethyl Orthosilicate (TEOS; Si(C$_2$H$_5$O)$_4$; Sigma-Aldrich, 98 %) and Methyl-triethoxysilane (MTES; CH$_3$-Si(C$_2$H$_5$O)$_3$; Sigma-Aldrich, 99 %) were used as silicon precursors, mixed in a molar fraction of 40 % TEOS and 60 % MTES. Grade 4 COOH-functionalized graphene nanoplatelets (figure 1), with thickness values lower than 4 nm and 1-2 μm wide, provided by Cheap Tubes Inc, were added to four coatings in different concentrations: 0.005 wt. %, 0.05 wt. %, 0.5 wt.% and 1 wt.%. The fifth coating was not doped. The sols were synthesized using isopropanol (Sigma-Aldrich, ≥ 98 %) as organic solvent and 0.1 M HCl (Sigma-Aldrich, 37 %) catalyst to control the hydrolysis and polycondensation reactions during the synthesis. All the sol-gels were generated with the same molar ratio of the reagents (1:5:10), *i.e.*, 1 mol of precursors (40% TEOS / 60% MTES), 5 mols of Isopropanol, and 10 mols of 0.1HCl distilled water.
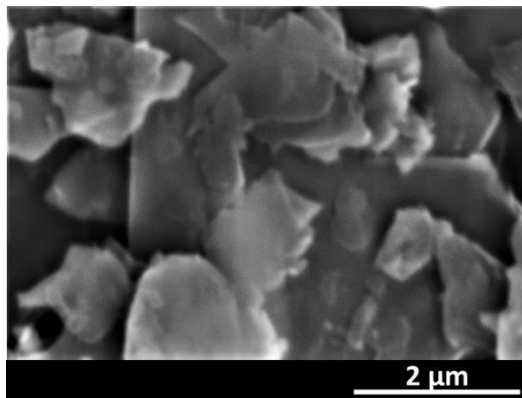

Figure 1. SEM micrograph of the COOH-GNPs used as nanocharges in the different sol-gels.

The synthesis process of the sols for the different coating systems was as follows (figure 2): five mixtures of TEOS and MTES with the specified molar ratio were generated in five different beakers under magnetic stirring at room temperature for 10 minutes. While the silicon precursors were mixing, the calculated mass of COOH-GNPs for each coating was added to four different beakers containing the calculated volume of isopropanol (B: 0.005 wt.% GNPs, C: 0.05 wt.% GNPs, D: 0.5 wt.% GNPs and E: 1 wt.% GNPs), no GNPs were added to the fifth

beaker (A), used for the generation of the non-doped coating. The beakers containing the four different COOH-GNPs concentrations were immersed in an ultrasonic bath for 10 minutes for the dispersion of the nanocharges in the isopropanol. After this time, the isopropanol without nanocharges, and the four mixtures of COOH-GNPs and isopropanol, were poured into the previously mixed TEOS/MTES mixture and then stirred for 10 minutes. After this process, the calculated volume of 0.1 M HCl was dropwise added to each TEOS/MTES – isopropanol mixture while stirring. Once all the reagents were added to the five different sols, they were stirred for 2 hours at room temperature to let the hydrolysis and polycondensation reactions take place. Finally, the sol-gels were left to stand for 30 minutes to let the reactions be completed before the coating of the AZ31 substrates.
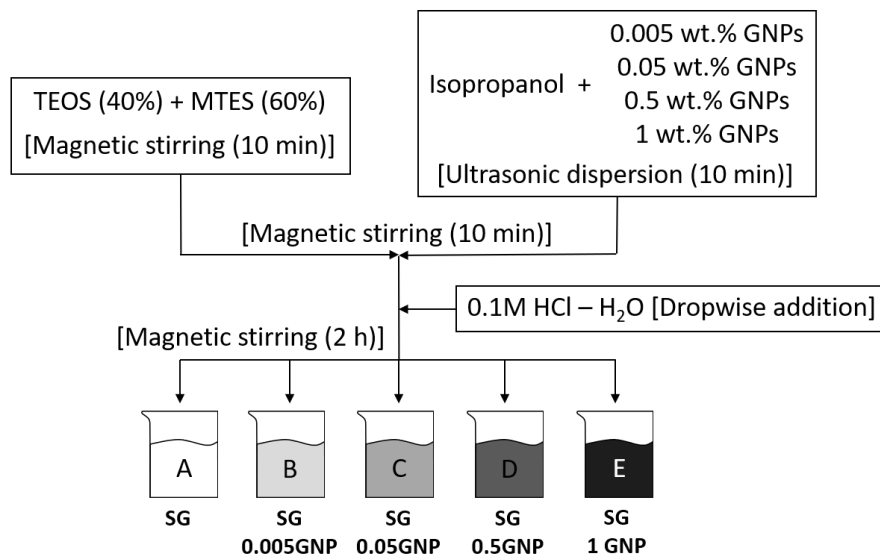

Figure 2. Sol-gel synthesis process scheme.

To minimize the aggregation of the GNPs, the AZ31 substrates were coated by the dip-coating method immediately after the synthesis of the sol-gels. Moreover, regarding the minimization of the aggregation of GNPs, the sol-gels were magnetically stirred before coating each sample. The samples were immersed in the corresponding sol-gel for 1 minute and then extracted at a controlled withdrawal speed of 35 cm/min. Finally, a two-step thermal treatment was applied to the coated samples. The first step consisted of a drying process at 100 ºC for 24 hours,

followed by the second step, a sintering process carried out at 200 ºC for 24 hours. After that, the samples remained in the oven until the room temperature was slowly reached to prevent the generation of internal stress that could crack the coatings.

2.3   Coating characterization

Previous to any test, the thickness and the homogeneity of the different coating systems, as well as the presence of the graphene nanoplatelets embedded in the coatings were evaluated by scanning electron microscopy (SEM – Hitachi S-3400N – 15 kV accelerating voltage, secondary electrons (SE) and backscattered electrons (BSE)). A sputter coating process was applied (Emitech K500X sputter coater) to generate a conductive ultrathin gold (Au) layer on the samples to facilitate the SEM evaluation. Due to the nature of the coating, it was difficult to prepare the samples to assess the thickness of the coatings in cross-section view. The samples were cut in half and the edge of the coating-substrate interface was slightly grounded to broke the coating. Then, the samples were tilted 60º, and thickness measurements were done. However, the real thickness values were obtained by applying a trigonometric correction. After the corrosion tests, cross-section micrographs of the tested samples were evaluated by SEM to understand the evolution of the corrosion process that occurred during the testing time in all the samples. Also, optical microscopy was used to evaluate the surface of the studied samples after 168 hours immersed in Hanks' solution.

2.4   Corrosion assessment

Three different *in vitro* experiments were carried out to assess the corrosion protection provided by the different coating systems. In all cases, the samples were immersed in Hank's solution as a liquid medium simulating the biological environment. Electrochemical linear polarization resistance (*Rp*) tests (Metrohm Autolab PGSTAT302N) were developed using a three-electrode cell configuration, using an Ag/AgCl reference electrode, a graphite rod as the counter electrode, and the coated samples as the working electrode. The samples were immersed in

Hanks' solution for 7 days and measurements were done every 24 hours of immersion. After 1 h of stabilization time, the samples were polarized ±10 mV around the E_{corr} value, with a scanning rate of 1 mV/s.

Electrochemical anodic-cathodic polarization tests were also carried out using the same cell configuration as in the case of the polarization resistance tests. After 1 h of stabilization time, a polarization range of 1000 mV (–400 mV, +600 mV) was applied to the samples around the E_{corr}, with a scanning rate of 1 mV/s. AC polarization tests were carried out after 24 hours of immersion. Due to the existence of the negative difference effect (NDE) in the magnesium alloys, the cathodic Tafel extrapolation was used to analyze the potentiodynamic curves. This method is used in the literature [37, 38] as a reliable method for estimating the actual corrosion rate of magnesium alloys.

2.5   Cytocompatibility assessment

Previous to any cytocompatibility test, the samples were sterilized. The sterilization protocol was as follows: (i) Three baths in ethanol 70 %, 10 minutes each. (ii) Three baths in distilled water, 10 minutes each. (iii) Bath in sterilized distilled water and ultraviolet radiation, 20 minutes each side of the sample. (iv) Bath in sterilized distilled water, 10 minutes. (v) Bath in minimum essential medium eagle, α modification (α-MEM) (A10490, Gibco) without ascorbic acid, for 10 minutes. (vi) Bath in complete culture medium, *i.e*., α-MEM + 10% fetal bovine serum (FBS) +1 % antibiotic (penicillin/streptomycin), 24 hours at 37 ºC.

After this procedure, the samples were ready for the cell culture. In this research, *in vitro* cytocompatibility was evaluated using an MC3T3-E1 preosteoblastic cell line (ATCC® CRL-2593™). This cell line was cultured in complete α-MEM and incubated at 37°C with 5% CO_2. A density of $4 \cdot 10^4$ cells/cm^2 were seeded on the surface of each sample and covered with 2 mL of complete culture medium. The medium was not maintained over the whole experimentation time.

To assess the cytocompatibility of the different coatings, three different tests were carried out. The metabolic activity of the cultures was assessed by the AlamarBlue test (Thermo Fisher). This test is a non-toxic procedure that allows evaluating the mitochondrial activity of the living cells to quantitatively assess cell proliferation. It is based on the cellular metabolic reduction of resazurin, a low fluorescent blue dye, into resorufin, which is highly fluorescent. In this test, the AlamarBlue dye was added to the culture medium (10 % of the culture medium volume) and then the samples were incubated for 90 minutes at 37 ºC. Then, the culture mediums of each sample containing the metabolites of the mitochondrial activity (resorufin) were collected and its fluorescence was measured using a microplate reader (Biotek, Synergy HT). These measurements were carried out in triplicate for each coating condition and at two different time points, after 72 hours and 168 hours after the cells seeding. The culture medium was refreshed after the measurements at 72 hours of experimentation.

The DNA quantitation test was carried out using the blue-fluorescent Hoechst 33258 nuclei acid stain, following the protocol provided by the manufacturer (Thermo Fisher, FluoReporter®). This is a destructive test. Therefore, the measurement was carried out only 168 hours after the cell seeding. The fluorescence for each sample was evaluated using the microplate reader (Biotek, Synergy HT). The culture medium was not refreshed during the 168 hours of cell culture.

An inverted fluorescence microscope (Olympus IX51) was used to assess the adhesion, morphology, and growth of the pre-osteoblastic cells on the different coatings. To obtain fluorescent micrographs of the cultures, immunocytochemistry staining of the DNA and the actin filaments was carried out to respectively reveal the nucleus and the cytoskeleton of the cells. The DNA staining was achieved with Hoechst 33258 and the actin staining was obtained using Texas-Red X phalloidin (Thermo Fisher) following the manufacturer's orders. Previous to the staining, it was necessary for the cell culture fixation and the permeabilization of the cell wall, to let the fluorescent markers get into the cell cytoplasm. For this purpose, 1 mL of

formalin 10 % was added to each sample and fixed for 15 min. After that, the samples were rinsed with 1 mL of phosphate-buffered saline (PBS), and then the samples were covered with Triton X-100 0.1% (v/v) for 5 minutes to make the cell membrane permeable to the dyes. Once stained, the samples were evaluated in the fluorescence microscope using $\lambda_{ex} = 380$ nm and $\lambda_{em} = 445$ nm for Hoechst, and $\lambda_{ex} = 550$ nm and $\lambda_{em} = 600$ nm for actin.

Statistical analysis was carried out for the metabolic activity and DNA quantitation tests (average value ± standard deviation), with a confidence interval of 95% ($p < 0.05$) consisting of one-way ANOVA and Tukey's post hoc tests.

3. Results

3.1 Coating characterization

The thickness of the different coatings was assessed using scanning electron microscopy. Figure 3 shows the tilted view of the different coatings deposited on the AZ31 magnesium substrates, unveiling the thickness of the coatings. After a trigonometric correction, the average thickness values and the deviations are shown in figure 4.

The graph in figure 4 shows a trend in which higher thickness values were reached for the coatings with the bigger concentrations of COOH-GNPs. However, for the highest COOH-GNPs concentrations, 1 wt. % and 0.5 wt. %, SEM micrographs show that GNPs aggregates were formed embedded inside the coatings (figure 5). In these cases, the presence of these aggregates led to the generation of cracks, likely produced during the drying of the coatings due to the generation of stress between the aggregates and the coating material.
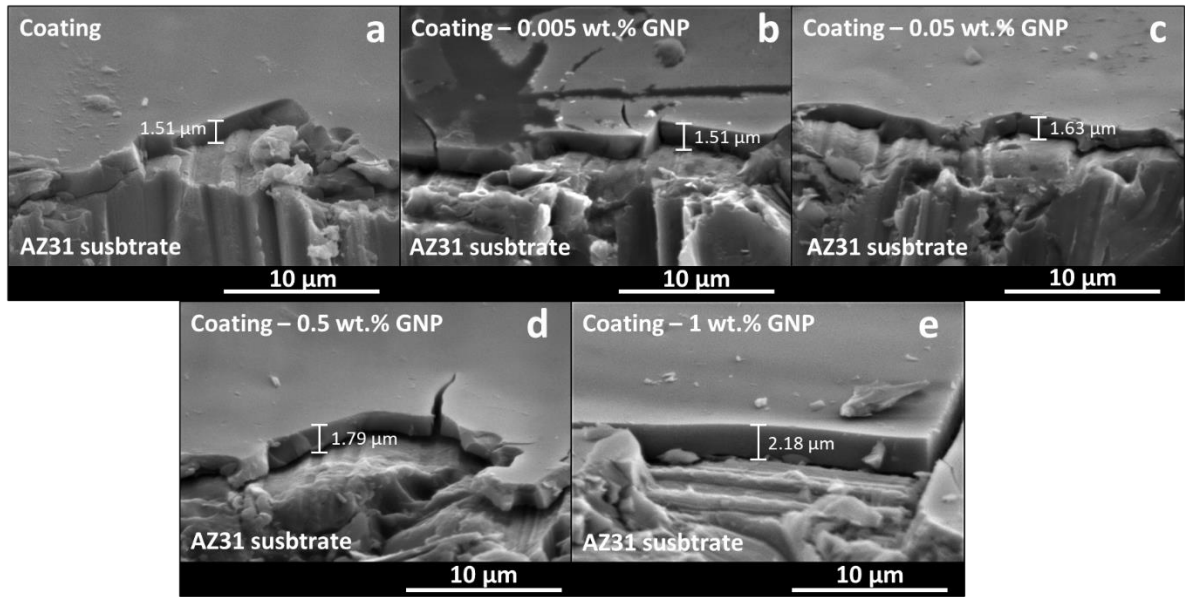
Figure 3. 60° Tilted view of the different coatings deposited on AZ31 magnesium substrates. (a) Sol-gel without nanocharges, (b) Sol-gel + 0.005 wt. % GNPs, (c) Sol-gel + 0.05 wt. % GNPs, (d) Sol-gel + 0.5 wt. % GNPs and (e) Sol-gel + 1 wt. % GNPs.

The presence of these aggregates and the subsequent cracks also modified the surface morphology of these coatings, which were less smooth than the coatings loaded with lower COOH-GNPs concentrations. COOH-GNPs aggregates were also found in the coating with a concentration of 0.05 wt. % of nanocharges. However, in this case, no significant cracks were generated around these aggregates.
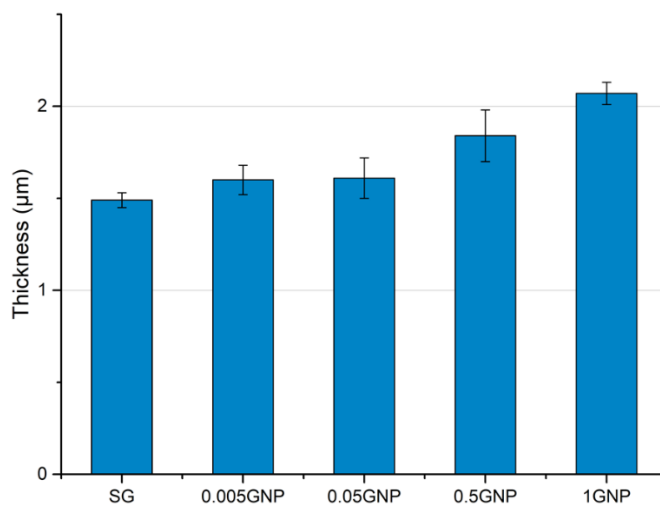

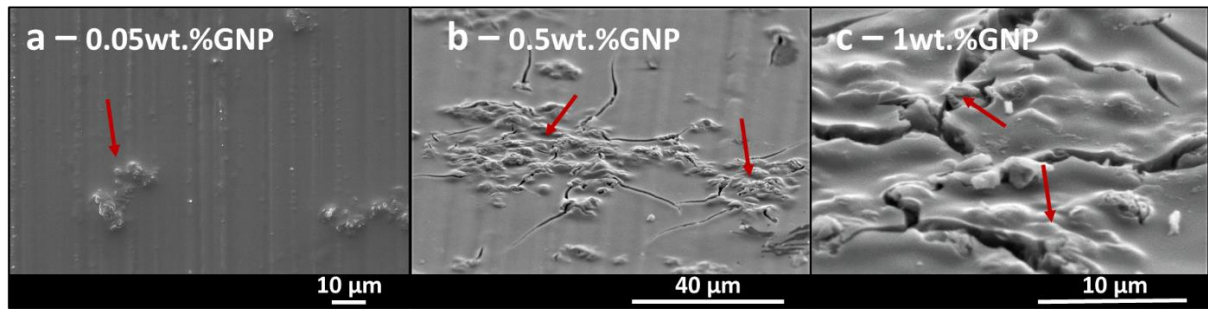Figure 4. Thickness values for all the different coating systems.

Figure 5. COOH-GNPs aggregates embedded in the sol-gel coatings with the highest GNP concentrations. (a) non-cracked 0.05 wt.% sol-gel, (b) cracked 0.5 wt.% sol-gel and (c) cracked 1 wt.% sol-gel.

3.2   Linear polarization resistance

The results of the linear polarization resistance tests are shown in figure 6. At the beginning of the experimentation time (1 hour of immersion), the coatings loaded with the lower COOH-GNPs concentrations (0.005 wt.% and 0.05 wt.%) have polarization resistance values two orders of magnitude higher than the values for the bare AZ31 substrate, and this tendency is maintained at all tested times, even after 7 days. The sol-gel coating without nanocharges shows lower polarization resistance values than the previous coatings, but still one order of magnitude higher than the bare substrate. An interesting result is provided by the coating with the highest concentration of nanocharges (1 wt.%). In this case, after 1 hour of immersion, the polarization resistance value of this coating was higher, but in the same order of magnitude, than the value for the AZ31 bare substrate.

Over the experimentation time, fluctuations can be seen for almost all the coating conditions and the bare substrate.
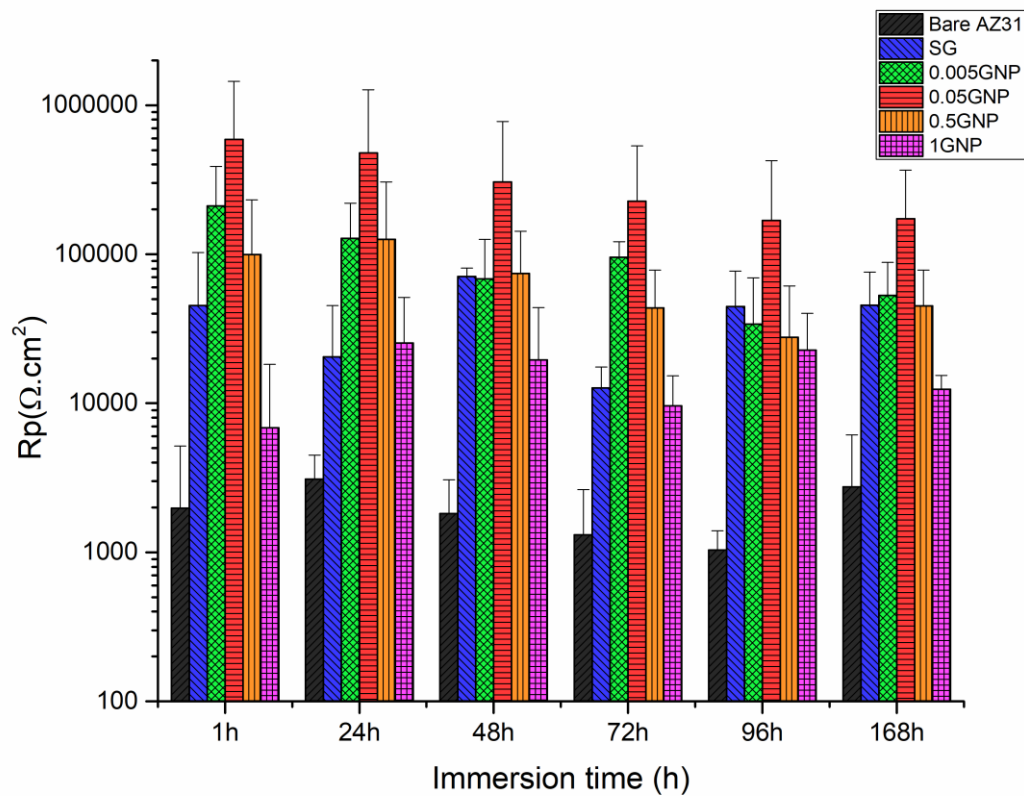
Figure 6. Linear polarization values for the different coating conditions and the bare substrate immersed in Hanks' solution for 168 hours.

Finally, figure 7 shows optical macrographs of the surface of the different tested samples after 168 h of immersion in Hanks' solution. The surface of the sample protected with the sol-gel coating without nanocharges (SG) appears less affected than the bare AZ31 substrate. Then, as the concentration of GNPs increases in the sol-gel coatings, the samples appear less affected, as it can be seen for the samples with the sol-gel coatings doped with 0.005 wt.% GNP and 0.05 wt.% GNP, reaching the highest protection at this point. However, the use of GNPs concentrations higher than 0.05 wt.% results in a decrease in the protection provided by the sol-gel coatings. Thus, the samples protected with the sol-gel coatings doped with the highest GNPs concentrations (1 wt.% and 0.5 wt.%) appear even more affected than the sample protected with the sol-gel coating without nanocharges.
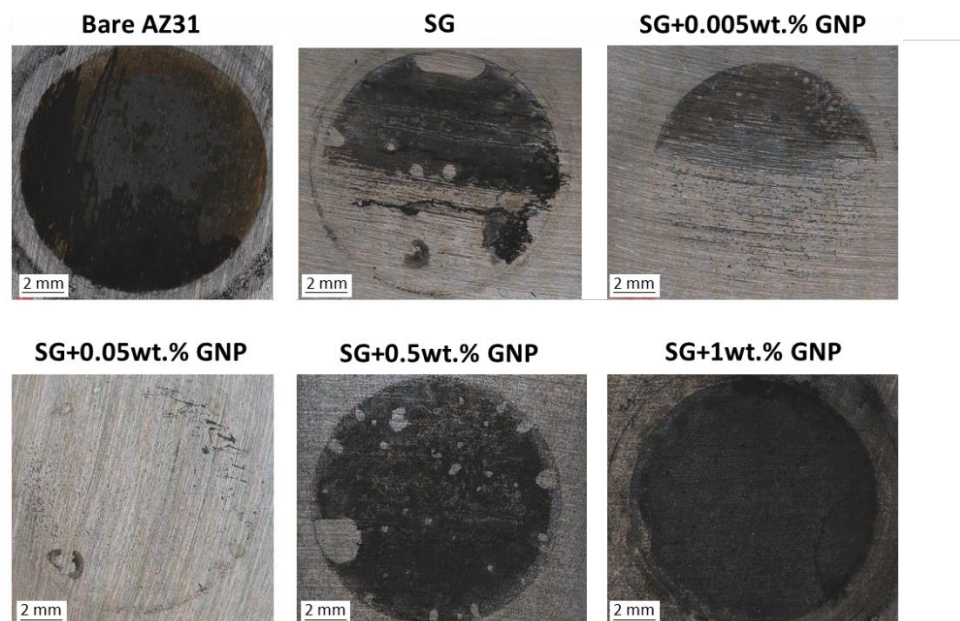
Figure 7. Photographs of the surface of the different samples after immersion in Hanks'
solution for 168 hours.

3.3   Anodic-Cathodic polarization

The measurements of the anodic-cathodic polarization were carried out after 24 hours of immersion. Figure 8 shows a representative example of the anodic-cathodic curves for all the tested conditions and Table II shows the E_{corr} and current density (i) values for each condition extracted from the triplicates of the anodic-cathodic polarization tests using the cathodic Tafel extrapolation. As in the case of the polarization resistance, all the coating systems improved the corrosion protection of the AZ31 alloy.

The lowest current density was obtained for the sol-gel coating with a COOH-GNPs concentration of 0.05 wt.%. It was one order of magnitude lower than the value of the bare AZ31 substrate and the coatings with the highest GNPs concentrations (1 wt.% and 0.5 wt.%), and lower, but in the same order of magnitude, than the coating without nanocharges and the coating with the lowest GNPs concentration (0.005 wt.%). Thus, this coating showed the most protective behavior as in the case of the polarization resistance tests.
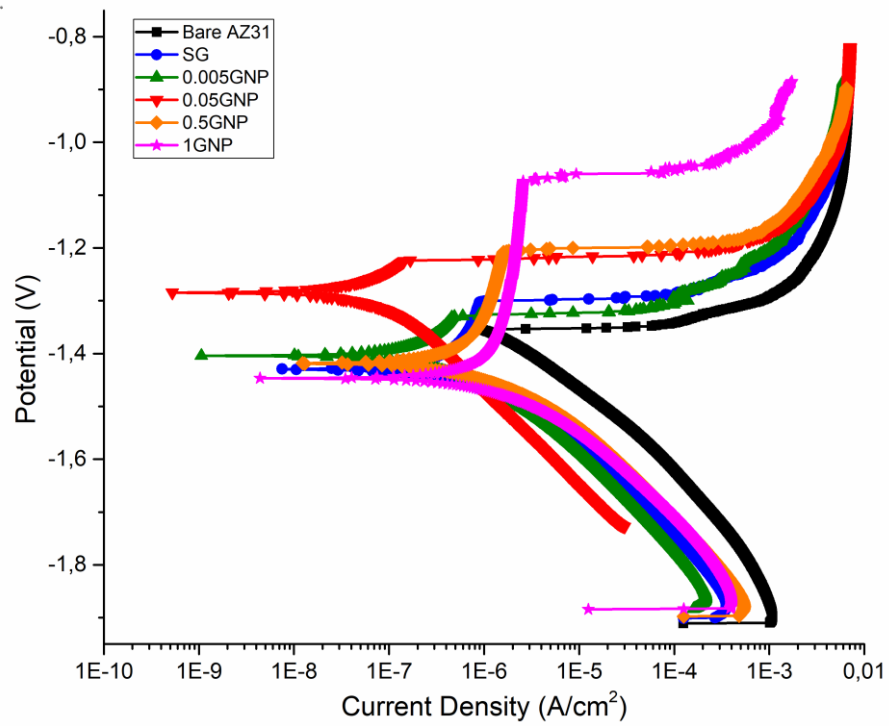
Figure 8. Anodic-Cathodic diagrams for the different coating conditions and the bare AZ31 substrate after 24 hours of immersion in Hanks' solution.

Table II. E_{corr} and current density values obtained by the cathodic Tafel extrapolation after 24 hours of immersion in Hanks' solution.

Sample	E_{corr} (V)	i (10^{-6} A/cm^2)
Bare AZ31	-1.36 ± 0.01	9.5 ± 0.4
SG	-1.40 ± 0.03	0.84 ± 0.02
0.005GNP	-1.36 ± 0.05	0.29 ± 0.01
0.05GNP	-1.34 ± 0.06	0.17 ± 0.08
0.5GNP	-1.40 ± 0.01	1.4 ± 0.9
1GNP	-1.43 ±0.03	1.6 ± 0.4

After 24 hours of immersion, the sol-gel coatings with the highest GNPs concentrations (1 wt.% and 0.5 wt.%) showed the highest current densities of all the coating conditions.

3.4 Immunofluorescence microscopy

An immunocytochemistry staining (figure 9) for cytoskeleton (actin) and cellular nuclei (DNA) was used to assess the osteoblasts culture. Cell morphology analysis is frequently used to understand how the cells were distributed on the surface of the different samples, attending to several criteria such as spreading and monolayer formation.

In the case of the bare AZ31 substrate, although a big number of cells can be observed over the surface of the substrate, instead of being adhered and expanded, they were grouped forming cellular clusters. These cellular morphologies can be a consequence of poor adhesion and cell spreading on the surface of the bare substrate. In contrast, images demonstrated that all the coating conditions let the proliferation of the cell cultures at 168 hours from cell seeding. A dense cellular monolayer was grown in all the coating conditions and the cells showed alignment in concordance with the direction of the grinding lines of the underlying substrates. The generation of an osteoblastic monolayer is associated with the secretion of a specialized extracellular matrix. To generate bone matrix, osteoblastic cultures establish cellular junctions to coordinate the mineralization of the bone matrix, including the release of biological factors to the medium like collagen.
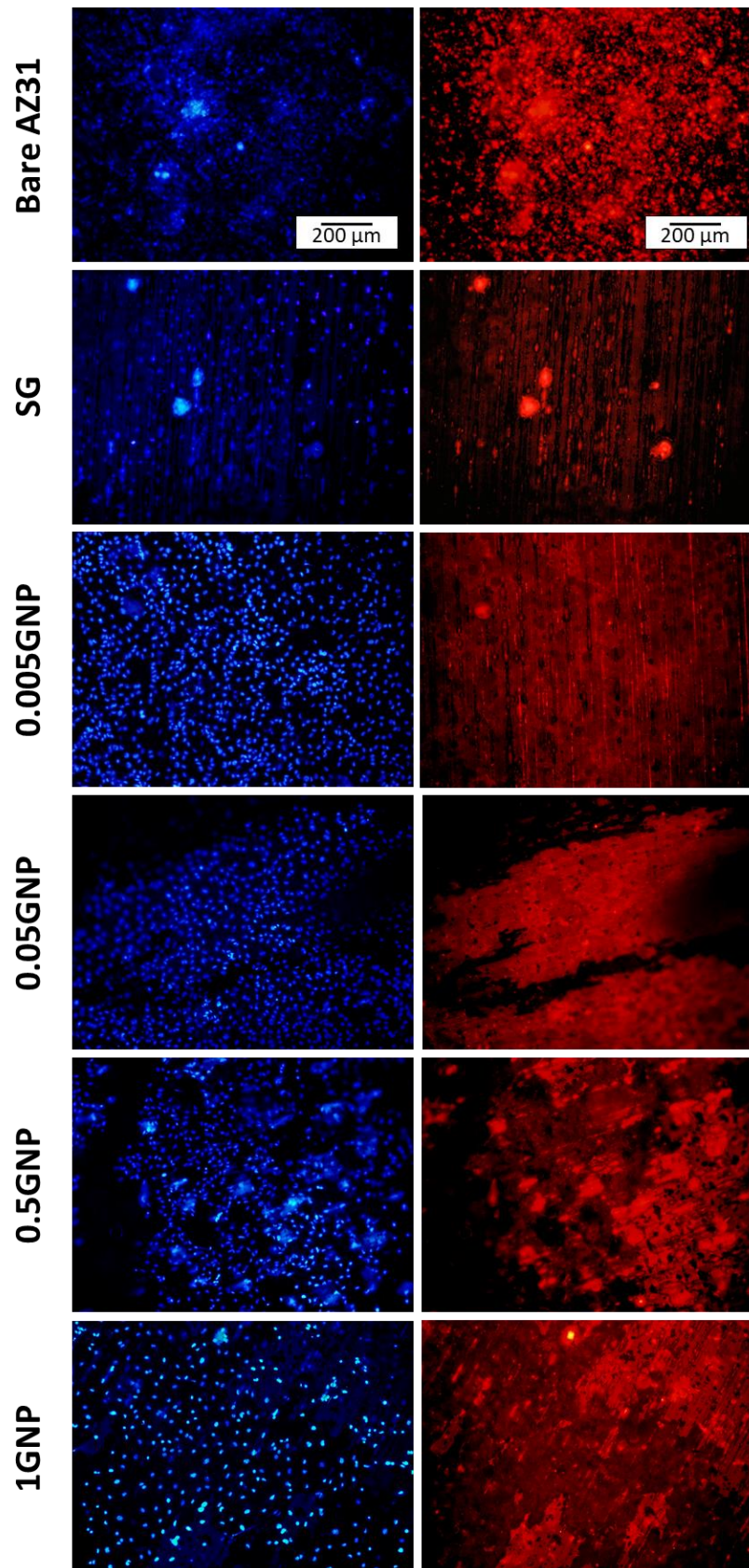
Figure 9. Immunofluorescence micrographs of the different cultures after 168 hours of experimental time. Blue images representing cell nuclei staining by Hoechst. Red images representing cell cytoskeleton by actin staining using phalloidin Texas-Red X

3.5 Metabolic Activity

Figure 10 shows the relative fluorescence units (RFU) extracted from the AlamarBlue tests for the different coatings and the bare AZ31 substrate after 72 hours and 168 hours of cell seeding. It is remarkable that, for both testing times, the highest values correspond with the samples which coatings were doped with the two highest COOH-GNPs concentrations (0.5 wt.% and 1 wt.%). In all cases, including the bare AZ31, the metabolic activity was increased between 72 hours and 168 hours of experimentation. Also, the highest increment in the metabolic activity between measuring times can be observed in the samples coated with the sol-gels doped with the highest COOH-GNPs concentrations.
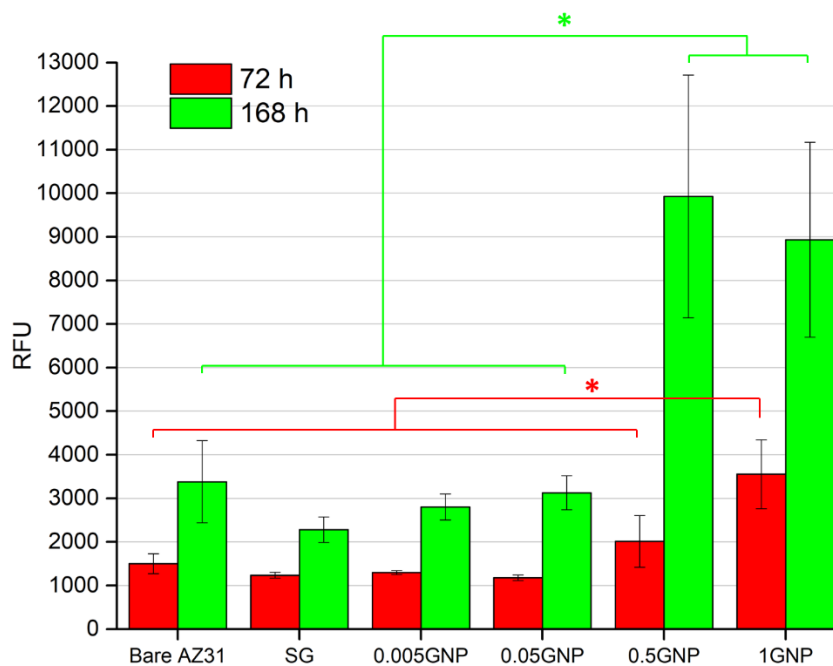
Figure 10. Relative fluorescence units from the AlamarBlue test after 72 hours and 168 hours. Significant differences are indicated by * ($p < 0.05$, ANOVA, Tukey's test).

3.6 DNA quantitation

Figure 11 shows the results obtained from the tests of the DNA quantitation using Fluoreporter assay in the samples coated with the different conditions, as well as in the bare AZ31 substrate. Measurements were done 168 hours after the cell seeding. Higher fluorescence values indicate

a higher amount of DNA and, therefore, a higher number of cells proliferating over the sample. In this experiment, the mean fluorescence values were very close for all the different conditions. The ANOVA and Tukey's tests resulted in no significant differences between all the studied samples. Thus, almost the same number of cells was present in all the samples, indicating that, after 168 hours of culture, the cell proliferation was almost the same both for all the coated conditions and for the bare AZ31 substrates.
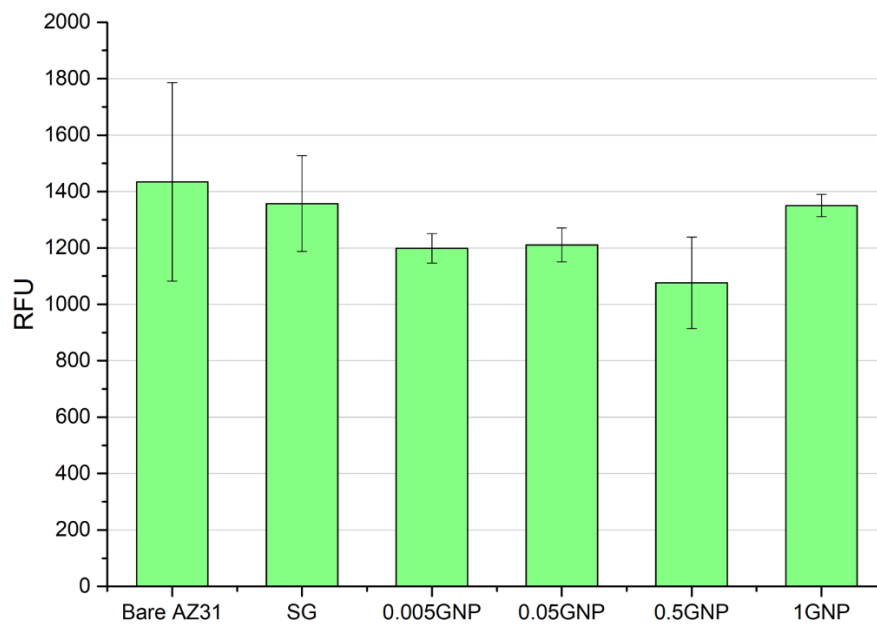

Figure 11. Relative fluorescence units from the DNA quantitation test after 168 hours of culture time. No significant differences were found in $p < 0.05$ ANOVA and Tukey's tests.

4.   **Discussion**

All the different coating systems deposited on AZ31 magnesium substrates improved the protection against in vitro corrosion when they were immersed in a biological simulated solution (Hanks' solution). However, as the coatings were doped with different concentrations of nanocharges (COOH-GNPs), their morphology and surface conditions were modified. The lack of nanocharges in the initial sol-gel, as well as the use of the lowest GNPs concentrations (0.005 wt.% and 0.05 wt.%), let to obtain coatings with thickness values around 1.5 μm, with

no visible defects nor cracks that could decrease the protective barrier effect of these coatings. However, an increment in the concentration of the nanocharges in the initial sol-gels, in the case of the coatings with the highest GNPs concentrations (0.5 wt.% and 1 wt.%), caused some changes in the morphology and properties of these coatings. The first consequence of the increment in the nanocharges concentration was an increment in the thickness of the coatings, this trend is visible in the graph of figure 4. This behavior is likely motivated due to changes in the viscosity of the initial sol-gels by the addition of higher concentrations of nanocharges [39]. As the substrates were coated by the dip-coating technique, the viscosity of the sol-gel, among other parameters like its density or the roughness and the withdrawal speed of the coated substrate, in the case of Newtonian liquids, influence the final thickness of the deposited coatings, as shown by the modified Landau-Levich equation (equation 2) [13, 40, 41].

$$h = 0.94 \; \frac{(\eta \cdot v)^{2/3}}{\gamma_{LV}^{1/6}(\rho \cdot g)^{1/2}} \; r \tag{2}$$

In this equation, η is the viscosity, v is the withdrawal speed of the substrate, ρ is the density of the solution, g is the gravity acceleration, γ_{LV} is the liquid-vapor surface tension, and r is the roughness parameter as a function of the roughness (Ra) of the coated substrate.

The other implication of the increment in the nanocharges concentration in the initial sol-gel is the formation of significant GNPs aggregates embedded in these coatings. As it is shown in figure 5, there are big differences between the coating doped with 0.05 wt.% COOH-GNPs, where small GNPs aggregates were properly embedded in the coating without generating any crack, and the coatings doped with 0.5 wt.% and 1 wt.% COOH-GNPs, where GNPs aggregates of tens of microns are present. In this last case, the aggregates are not well integrated nor embedded in the coating and their presence led to the generation of cracks. Likely because of the size of the aggregates, some edges and parts of them remained out of the volume of the deposited coating, and then, during the drying process and the subsequent loss of volume of the

coating, these aggregates became internal stress-concentration points leading to the generation of cracks and creating the irregular coating morphology shown in figure 5.

Regarding corrosion protection, the use of graphene nanoplatelets as nanoreinforcement demonstrated to be an effective way to increase the performance of protective films, increasing the mechanical resistance of the coatings where the nanoreinforcement concentration is adequate, and also delaying the corrosion process by making it more difficult for aggressive species like chlorides, oxygen, and water to pass through the protective coating and reach the surface of the underlying substrate [42]. However, it is important to study the optimal GNPs concentration that could enhance the protective properties of the coatings. In the present study, it is shown that, for low GNPs concentration, there is an upward trend in the corrosion protection provided by the sol-gel coatings, related to the increment in the GNPs concentration. However, the presence of high concentrations of COOH-GNPs in the coatings, contrary to improve their protective properties, decreases their anticorrosion behavior due to a bad dispersion of the nanocharges and the generation of big aggregates acting as crack-generation points.

This behavior was shown in the electrochemical corrosion tests (figure 6) and in the images of the surface of the tested samples (figure 7). Thus, in the results extracted from the linear polarization resistance (Rp) tests, the best anticorrosion behavior was provided by the sol-gel coating that was doped with the 0.05 wt.% concentration, with an Rp value slightly decreasing all over the experimentation time, but always remaining as the highest value.

On the other hand, the Rp values of all the other coating conditions, as well as the bare AZ31 substrate, suffered fluctuations during the experimentation time. These fluctuations can be attributed to the formation of corrosion products once the aggressive medium managed to reach the surface of the substrates. Thus, between 1 hour and 24 hours after immersion, the polarization resistance value increased for the bare AZ31 substrate, as well as for the coating

systems with the highest GNPs concentrations (0.5 wt.% and 1 wt.%) that were cracked, indicating the poor barrier effect of these coatings.

Finally, in the same period, the Rp values of the coatings with the lowest GNPs concentrations (0.005 wt.% and 0.05 wt.%) as well as the sol-gel coating without nanocharges decreased, showing a slight loss of barrier effect, but still not being affected by the formation of corrosion products on the surface of the coated substrates. From 24 hours of immersion onwards, the polarization resistance values of the different samples fluctuated as the corrosion products were formed. However, in the case of the sol-gel coating doped with 0.05 wt.% COOH-GNPs, the polarization resistance value followed a downward trend but remained the highest value for all the immersion times showing the best anticorrosion protection of all the coating systems.

At the end of the experimentation time, the sol-gel coating doped with the highest GNPs concentration showed the lowest Rp value of all the coating systems. Therefore, it provided the lowest corrosion protection. In contrast with the sol-gel coating doped with 0.05 wt.% COOH-GNPs that provided the best anticorrosion behavior in this experiment. Figure 7 shows the degradation on the surface of the tested samples after the polarization resistance test. The surface of the sol-gel coating doped with 0.05 wt.% COOH-GNPs was not affected. Only small signs were visible, indicating the initiation of the degradation process. This sample showed the highest Rp value, and the minor damage can be correlated with the slight decrease of the Rp values for this sample with time (figure 6). Figure 7 also shows the relation between the concentration of nanocharges and the protective behavior of the coatings. Thus, the protective behavior increases as the GNPs concentration increases, until the optimal concentration was reached at 0.05 wt.%, obtaining the most protective coating. However, contrary to the previous trend, the addition of GNPs at higher concentrations than 0.05 wt.% resulted in a decrease in the protective behavior of the coatings. The presence of cracks promotes localized corrosion, and even the presence of GNPs may form a galvanic couple that would accelerate the corrosion

process. That is why the samples treated with the coatings with the highest GNPs concentrations show the highest degradation on their surface in figure 7.

The anodic-cathodic polarization data (**table II**) shows that the coatings act as protective barriers impeding the pass of current density after 24 hours of immersion in the simulated biological fluid. The data show that all the coating conditions improved the protection against corrosion, decreasing the pass of current density compared with the bare AZ31 substrate, especially in the case of the coating doped with 0.05 wt.% GNPs, showing a current density value almost two orders of magnitude lower than the bare AZ31 substrate. Moreover, the corrosion potential for this sample became less electronegative than the value of the bare substrate. As in the case of the linear polarization tests and the images in figure 7, this coating shows the best anticorrosion protective properties.

As it can be expected from the images in figure 5, the presence of cracks and irregularities in the coatings doped with the highest GNPs concentrations (1 wt.% and 0.5 wt.%) causes a decrease in the corrosion protection provided by these coatings. Thus, even they improved the protection compared with the bare substrate, they also show the highest current density values of all the coating conditions. This behavior was in concordance with the linear polarization results and the images of all the tested conditions shown in figure 7. The application of the different coatings promoted changes in the corrosion potential. The samples protected with the different sol-gel coatings present pitting potentials, but this behavior was not observed for the bare AZ31 substrate. This behavior can be explained because the unstable oxide layer that forms naturally on the bare AZ31 substrate does not provide any protection after 24 hours of immersion in the electrolyte.

Figure 12 shows the cross-section micrographs of all the tested conditions after 168 hours of immersion in Hanks' solution and is helpful to understand the corrosion process suffered for each sample. The red arrows indicate the presence of corrosion products, and the white arrows indicate the presence of sol-gel coating. In the case of the bare substrate (figure 12a), thick

accumulations of corrosion products can be found and generalized corrosion is found spread all over the sample surface.
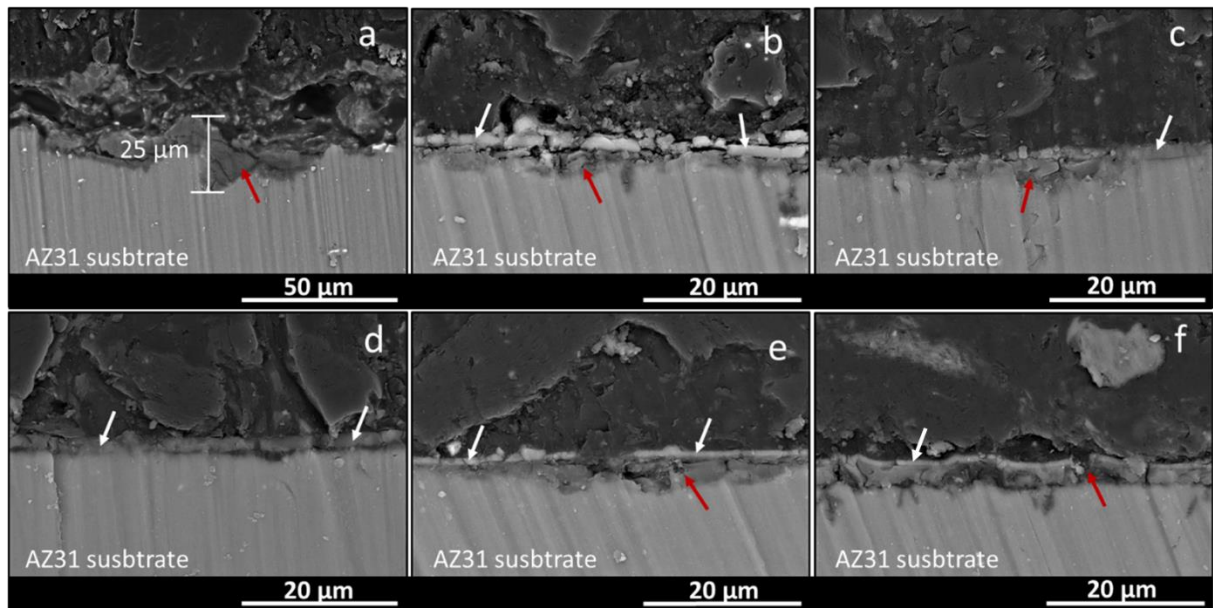

Figure 12. Cross-section micrographs of the samples after 168 h of immersion in Hanks' solution. (a) Bare AZ31 substrate, (b) sol-gel coating, (c) sol-gel coating with 0.005 wt.% GNPs, (d) sol-gel coating with 0.05 wt.% GNPs, (e) sol-gel coating with 0.5 wt.% GNPs and (f) sol-gel coating with 1 wt.% GNPs. Red arrows indicate corrosion products and white arrows indicate sol-gel coating.

The presence of a coating on the surface of the substrate induces a different corrosion process than in the case of the bare substrate. In that case, once the coatings start degrading at some points, small zones of the substrate are exposed to the aggressive medium. Thus, pitting corrosion starts at these points. This behavior can be observed in the anodic branch of the coated samples during the anodic-cathodic test, but not for the bare AZ31 (figure 8). Once the corrosion is initiated, differential aeration cells are created and the corrosion products start to grow and spread in the interface between the coating and the substrate. The corrosion products growing in this interface break the coating above generating cracks and detaching parts of the coating, and exposing new zones of the substrate to the aggressive medium. This behavior can be seen in figure 12e, where parts of the remaining coating are still visible on a layer of

corrosion products that were growing in the coating-substrate interface. In the center of the image, a zone can be seen where there is a lack of coating, where the pitting corrosion was likely initiated. Thus, instead of only generalized corrosion, pitting corrosion is commonly found in the coated samples as the first step for a total degradation of the coating.

This behavior was found in all the different coating conditions. However, the degradation rate was different depending on the concentration of nanocharges in the sol-gel coatings. Thus, as previously exposed, the highest GNPs concentrations (0.5 wt.% and 1 wt.%) led to thicker but cracked coatings, whose protection against corrosion was lower both in the electrochemical tests and in the images of their surfaces after the immersion in the Hanks' solution (figure 7). The SEM micrographs show thicker layers of corrosion products for these samples (figures 12e and 12f), indicating that the corrosion process was initiated earlier than in the other coated samples. Therefore, the progression of the corrosion was more widespread for these samples.

In the case of the sol-gel coating without nanocharges (figure 12b), and the coating doped with 0.005 wt.% GNPs (figure 12c), corrosion products are also present in the coating-substrate interface. However, the thickness of these corrosion layers is lower than in the case of the coatings with the highest nanocharges concentration, indicating a delay in the starting of the corrosion process for these conditions.

Finally, as shown in all the different tests and images, also in the SEM micrographs is possible to appreciate that the presence of the sol-gel coating doped with 0.05 wt.% GNPs (figure 12d) improved significantly the protection against corrosion. In this case, although the coating is cracked and detached from the substrate at some points, no significant corrosion products layer is visible, indicating that, at least until 168 hours of immersion, this coating can provide effective corrosion protection and significantly delay the corrosion process of the coated AZ31 substrate, being the most interesting coating system in terms of degradation rate control. The 0.05 wt.% GNPs concentration was found optimal to improve the protective properties of the sol-gel coatings. These nanocharges improve the anticorrosion behavior by two different

mechanisms. First, as they are embedded in the sol-gel coating, they act as obstacles inside the coatings, hindering the aggressive ions from the electrolyte to reach the surface of the magnesium substrate and increasing their pathway to the surface [31, 42]. Moreover, the addition of graphene nanoplatelets is known to improve the mechanical properties of coatings. Thus, a good GNPs dispersion can help to avoid the generation of cracks in the sol-gel coatings and, therefore, an enhancement in the barrier effect of the coatings [39].

Regarding cytocompatibility, the immunofluorescence micrographs in figure 9 are helpful to have a complete overview of what happens to the cell cultures seeded on the different coatings. Looking at these images it is possible to assure that the cell cultures proliferated in all the conditions, even in the case of the bare substrate, despite the changes in the pH caused by the liberation of H_2 during the corrosion of the magnesium alloy. However, there are morphological differences in the cultures depending on the samples. In the case of the cell nuclei staining micrographs (blue), it is possible to see that for all the coating conditions, nuclei appear as independent dots, indicating that the cells are neither stacked nor overlapped, that means the generation of a cell monolayer which is indicative of a good cytocompatibility. On the other hand, in the case of the bare substrate, the same amount of cell nuclei can be observed. However, in this case, the nuclei appeared overlapped and crowded, indicating that the cells are stacked in tridimensional structures instead of well adhered and spread on the surface of the bare substrate, which is indicative of the negative response of the culture in terms of adhesion and proliferation, at least for the experimentation time.

Cytoskeleton staining micrographs (red) corroborate this behavior. Thus, the fluorescence can be observed all over the surface of the samples with the different coatings, indicating that the cells have their cytoskeleton well spread, which means that they were well adhered to the surface, forming a cellular monolayer on these samples. However, in the case of the bare substrate, the cells presented round morphologies indicating that they are not expanded and,

therefore, not adhered to the substrate. Moreover, they generated big cellular groups that demonstrate active cell-to-cell junctions, but a poor level of cell-to-surface interactions.

Although the presence of the GNPs embedded in the coatings modified the surface topography, making these coatings less smooth and, in some cases, decreasing the protective properties of the coatings in terms of corrosion prevention, in terms of cytocompatibility, the roughness of the surface of the coatings can provide a positive effect for cellular adhesion because the roughness and the surface topology are factors that influence the adhesion and creation of a cellular monolayer [43, 44]. This could be one of the reasons why the metabolic activity is significantly increased in the case of the coatings doped with the highest GNPs concentrations (0.5 wt.% and 1 wt.%) (figure 10), since these coatings presented higher irregularities on their surfaces and were less smooth than the other coating systems. However, instead of direct measurement, the metabolic activity tests provide an indirect determination of the number of cells in the culture, by measuring the products of the metabolic processes of the cells. However, high metabolic activity can also be indicative of an accelerated cellular metabolism without a high proliferation of the culture, due to external factors affecting the cells. This fact is important because when the metabolic activity results are compared with the DNA quantitation tests (figure 11), there are significant differences in the behavior of the cell cultures seeded on the coatings with the highest GNPs concentrations.

Contrary to the metabolic activity tests, the DNA quantitation tests measure the amount of DNA present in the culture. Thus, higher fluorescence values can be directly correlated with a higher number of cells in the culture. However, no significant differences in terms of cell culture growth can be extracted from the DNA quantitation test between all the tested conditions, including the bare AZ31 substrate.

Thus, the higher metabolic activity values obtained for the coatings with the highest GNPs concentrations, instead of being a consequence of higher cell proliferation, as it can be discarded from the DNA quantitation tests, can be explained due to several factors. The first is that, as it

has been shown in the different electrochemical tests, the samples with the highest GNPs concentrations present lower protection against corrosion, even knowing that the corrosion behavior in Hanks' may be different from the behavior when the samples are immersed in the culture medium (α-MEM). However, the degradation rate of these samples was also higher during the cytocompatibility tests, and the liberation of H_2 to the culture medium during the corrosion process led to changes in the pH of the culture medium, detected by changes in the color of the media containing the bare substrate, as well as the coatings with the highest GNPs concentrations. Thus, changes in the initial conditions of the culture may affect the way that the cells behave, accelerating their metabolism as a response to these changes, but not promoting their proliferation.

Some studies suggest that carbon nanoparticles like graphene oxide could be cytotoxic to some extent, depending on the studied cell line and also on the concentration of these nanoparticles in the culture medium, promoting cellular oxidative stress phenomenon that can harm the cells and lead to a negative response of the culture [45 – 47]. Thus, the highest GNPs concentrations may elicit a cellular response to these nanoparticles, increasing the metabolic activity of the cells in these cultures. The high GNPs concentration factor seems to be responsible for the highest metabolic activity of the samples with higher GNPs concentrations because, in the case of the bare substrates, there are also changes in the pH of the culture medium, but the metabolic activity for these samples was closer to the values of the other coatings with lower GNPs concentrations of without nanocharges.

Therefore, the results of the cytocompatibility tests show that, even if these cells can proliferate in the presence of an AZ31 base substrate, it is necessary to apply a coating to promote cell adhesion and monolayer formation. The sol-gel coating doped with 0.05 wt.% COOH-GNPs has demonstrated the best balance between degradation control and improvement of the cytocompatibility.

5.   Conclusions

The objective of this research is to assess the right COOH-GNPs concentration that is necessary to add to silica sol-gels to generate coatings that provide the best corrosion degradation rate control while presenting improved cytocompatibility for preosteoblastic cells, in order to generate treatments for biodegradable implants intended to be used in the treatment of bone fractures.

A concentration of 0.05 wt.% functionalized COOH-GNPs was found optimal to significantly improve the protection against corrosion and to delay the beginning of the degradation process, which could help to maintain the mechanical properties of the implant until the healing process of the natural bone is started, decreasing the possibility of mechanical failure of the implant.

Regarding biocompatibility, low COOH-GNPs concentrations, like the 0.05 wt.%, have shown good metabolic activity and DNA quantitation results, as well as proper adhesion and cellular monolayer generation as initial steps for the MC3T3 preosteoblasts to generate bone matrix. Showing promising results of these coating treatments for the generation of osteoconductive biodegradable implants.

Higher concentrations of COOH-GNPs led to the generation of cracked coatings with low corrosion protection properties. Regarding cytocompatibility, these GNPs concentrations seem to affect the metabolic processes of the MC3T3 cell line, but did not affect cell culture proliferation.

References

[1]   F. Witte, The history of biodegradable magnesium implants: A review, Acta Biomater. 6 (2010) 1680–1692. https://doi.org/10.1016/j.actbio.2010.02.028.

[2]   H. Windhagen, K. Radtke, A. Weizbauer, J. Diekmann, Y. Noll, U. Kreimeyer, R. Schavan, C. Stukenborg-Colsman, H. Waizy, Biodegradable magnesium-based screw clinically equivalent to titanium screw in hallux valgus surgery: Short term results of the first prospective, randomized, controlled clinical pilot study, Biomed. Eng. Online. 12 (2013) 1. https://doi.org/10.1186/1475-925X-12-62.

[3]   S. Agarwal, J. Curtin, B. Duffy, S. Jaiswal, Biodegradable magnesium alloys for orthopaedic applications: A review on corrosion, biocompatibility and surface modifications, Mater. Sci. Eng. C. 68 (2016) 948–963. https://doi.org/10.1016/j.msec.2016.06.020.

[4]   Y. Xin, T. Hu, P.K. Chu, In vitro studies of biomedical magnesium alloys in a simulated physiological environment: A review, Acta Biomater. 7 (2011) 1452–1459. https://doi.org/10.1016/j.actbio.2010.12.004.

[5]   B.L. Mordike, T. Ebert, Magnesium Properties - applications - potential, Mater. Sci. Eng. A. 302 (2001) 37–45. https://doi.org/10.1016/S0921-5093(00)01351-4.

[6]   A.M. Rashmir-Raven, D.C. Richardson, H.M. Aberman, D.J. DeYoung, Response of cancellous and cortical canine bone to hydroxylapatite-coated and uncoated titanium rods, J. Appl. Biomater. 6 (1995) 237–242. https://doi.org/10.1002/jab.770060404.

[7]   J. Nagels, M. Stokdijk, P.M. Rozing, Stress shielding and bone resorption in shoulder arthroplasty, J. Shoulder Elb. Surg. 12 (2003) 35–39. https://doi.org/10.1067/mse.2003.22.

[8]   Z. Du, H. Leng, L. Guo, Y. Huang, T. Zheng, Z. Zhao, X. Liu, X. Zhang, Q. Cai, X. Yang, Calcium silicate scaffolds promoting bone regeneration via the doping of Mg^{2+} or Mn^{2+} ion, Compos. Part B Eng. 190 (2020) 107937. https://doi.org/10.1016/j.compositesb.2020.107937.

[9]   Z. Wang, Q. Liu, C. Liu, W. Tan, M. Tang, X. Zhou, T. Sun, Y. Deng, Mg^{2+} in β-TCP/Mg–Zn composite enhances the differentiation of human bone marrow stromal cells into osteoblasts through MAPK-regulated Runx2/Osx, J. Cell. Physiol. 235 (2020) 5182–5191. https://doi.org/10.1002/jcp.29395.

[10]   M.L. Zheludkevich, I.M. Salvado, M.G.S. Ferreira, Sol-gel coatings for corrosion protection of metals, J. Mater. Chem. 15 (2005) 5099–5111. https://doi.org/10.1039/b419153f.

[11]   Q. Li, Sol-gel coatings to improve the corrosion resistance of magnesium (Mg) alloys, Corros. Prev. Magnes. Alloy. A Vol. Woodhead Publ. Ser. Met. Surf. Eng. (2013) 469–485. https://doi.org/10.1533/9780857098962.3.469.

[12]   D. Wang, G.P. Bierwagen, Sol-gel coatings on metals for corrosion protection, Prog. Org. Coatings. 64 (2009) 327–338. https://doi.org/10.1016/j.porgcoat.2008.08.010.

[13]   J.P. Fernández-Hernán, A.J. López, B. Torres, J. Rams, Influence of roughness and grinding direction on the thickness and adhesion of sol-gel coatings deposited by dip-coating on AZ31 magnesium substrates. A Landau–Levich equation revision, Surf. Coatings Technol. 408 (2021). https://doi.org/10.1016/j.surfcoat.2020.126798.

[14] A.F. Galio, S. V. Lamaka, M.L. Zheludkevich, L.F.P. Dick, I.L. Müller, M.G.S. Ferreira, Inhibitor-doped sol-gel coatings for corrosion protection of magnesium alloy AZ31, Surf. Coatings Technol. 204 (2010) 1479–1486. https://doi.org/10.1016/j.surfcoat.2009.09.067.

[15] S. Radin, P. Ducheyne, T. Kamplain, B.H. Tan, Silica sol-gel for the controlled release of antibiotics. I. Synthesis, characterization, and in vitro release, J. Biomed. Mater. Res. 57 (2001) 313–320. https://doi.org/10.1002/1097-4636(200111)57:2<313::AID-JBM1173>3.0.CO;2-E.

[16] A.J. López, A. Ureña, J. Rams, Wear resistant coatings: Silica sol-gel reinforced with carbon nanotubes, Thin Solid Films. 519 (2011) 7904–7910. https://doi.org/10.1016/j.tsf.2011.05.076.

[17] R. Samadianfard, D. Seifzadeh, A. Habibi-Yangjeh, Sol-gel coating filled with SDS-stabilized fullerene nanoparticles for active corrosion protection of the magnesium alloy, Surf. Coatings Technol. 419 (2021) 127292. https://doi.org/10.1016/j.surfcoat.2021.127292.

[18] Y.J. Tarzanagh, D. Seifzadeh, Z. Rajabalizadeh, A. Habibi-Yangjeh, A. Khodayari, S. Sohrabnezhad, Sol-gel/MOF nanocomposite for effective protection of 2024 aluminum alloy against corrosion, Surf. Coatings Technol. 380 (2019) 125038. https://doi.org/10.1016/j.surfcoat.2019.125038.

[19] S.M. Ashrafi-Shahri, F. Ravari, D. Seifzadeh, Smart organic/inorganic sol-gel nanocomposite containing functionalized mesoporous silica for corrosion protection, Prog. Org. Coatings. 133 (2019) 44–54. https://doi.org/10.1016/j.porgcoat.2019.04.038.

[20] R. V. Lakshmi, S. Sampath, S.T. Aruna, Silica-alumina based sol-gel coating containing cerium oxide nanofibers as a potent alternative to conversion coating for AA2024 alloy, Surf. Coatings Technol. 411 (2021) 127007. https://doi.org/10.1016/j.surfcoat.2021.127007.

[21] A.L.K. Tan, A.M. Soutar, I.F. Annergren, Y.N. Liu, Multilayer sol-gel coatings for corrosion protection of magnesium, Surf. Coatings Technol. 198 (2005) 478–482. https://doi.org/10.1016/j.surfcoat.2004.10.066.

[22] Ö. Kesmez, E. Akarsu, H.E. Çamurlu, E. Yavuz, M. Akarsu, E. Arpaç, Preparation and characterization of multilayer anti-reflective coatings via sol-gel process, Ceram. Int. 44 (2018) 3183–3188. https://doi.org/10.1016/j.ceramint.2017.11.088.

[23] J.D. Maeztu, P.J. Rivero, C. Berlanga, D.M. Bastidas, J.F. Palacio, R. Rodriguez, Effect of graphene oxide and fluorinated polymeric chains incorporated in a multilayered sol-gel nanocoating for the design of corrosion resistant and hydrophobic surfaces, Appl. Surf. Sci. 419 (2017) 138–149. https://doi.org/10.1016/j.apsusc.2017.05.043.

[24] D. Arcos, M. Vallet-Regí, Sol-gel silica-based biomaterials and bone tissue regeneration, Acta Biomater. 6 (2010) 2874–2888. https://doi.org/10.1016/j.actbio.2010.02.012.

[25] A.L. Pierce, S. Sommakia, J.L. Rickus, K.J. Otto, Thin-film silica sol-gel coatings for neural microelectrodes, J. Neurosci. Methods. 180 (2009) 106–110. https://doi.org/10.1016/j.jneumeth.2009.02.008.

[26] I. Alfieri, A. Lorenzi, A. Montenero, G. Gnappi, F. Fiori, Sol-gel silicon alkoxides-

polyethylene glycol derived hybrids for drug delivery systems, J. Appl. Biomater. Biomech. 8 (2010) 14–19. https://doi.org/10.1177/228080001000800103.

[27]   E.J. Kim, S.Y. Bu, M.K. Sung, M.K. Choi, Effects of silicon on osteoblast activity and bone mineralization of MC3T3-E1 cells, Biol. Trace Elem. Res. 152 (2013) 105–112. https://doi.org/10.1007/s12011-012-9593-4.

[28]   R. Jugdaohsingh, Silicon and bone health, J. Nutr. Heal. Aging. 11 (2007) 99–110.

[29]   A.E. Porter, Nanoscale characterization of the interface between bone and hydroxyapatite implants and the effect of silicon on bone apposition, Micron. 37 (2006) 681–688. https://doi.org/10.1016/j.micron.2006.03.006.

[30]   S. Nezamdoust, D. Seifzadeh, rGO@APTES/hybrid sol-gel nanocomposite for corrosion protection of 2024 aluminum alloy, Prog. Org. Coatings. 109 (2017) 97–109. https://doi.org/10.1016/j.porgcoat.2017.04.022.

[31]   R. Ding, W. Li, X. Wang, T. Gui, B. Li, P. Han, H. Tian, A. Liu, X. Wang, X. Liu, X. Gao, W. Wang, L. Song, A brief review of corrosion protective films and coatings based on graphene and graphene oxide, J. Alloys Compd. 764 (2018) 1039–1055. https://doi.org/10.1016/j.jallcom.2018.06.133.

[32]   J.P. Fernández-Hernán, A.J. López, B. Torres, J. Rams, Silicon oxide multilayer coatings doped with carbon nanotubes and graphene nanoplatelets for corrosion protection of AZ31B magnesium alloy, Prog. Org. Coatings. 148 (2020) 105836. https://doi.org/10.1016/j.porgcoat.2020.105836.

[33]   D. Prasai, J.C. Tuberquia, R.R. Harl, G.K. Jennings, K.I. Bolotin, Graphene: Corrosion-inhibiting coating, ACS Nano. 6 (2012) 1102–1108. https://doi.org/10.1021/nn203507y.

[34]   C.H. Chang, T.C. Huang, C.W. Peng, T.C. Yeh, H.I. Lu, W.I. Hung, C.J. Weng, T.I. Yang, J.M. Yeh, Novel anticorrosion coatings prepared from polyaniline/graphene composites, Carbon N. Y. 50 (2012) 5044–5051. https://doi.org/10.1016/j.carbon.2012.06.043.

[35]   D. Depan, B. Girase, J.S. Shah, R.D.K. Misra, Structure-process-property relationship of the polar graphene oxide-mediated cellular response and stimulated growth of osteoblasts on hybrid chitosan network structure nanocomposite scaffolds, Acta Biomater. 7 (2011) 3432–3445. https://doi.org/10.1016/j.actbio.2011.05.019.

[36]   A. Aryaei, A.H. Jayatissa, A.C. Jayasuriya, The effect of graphene substrate on osteoblast cell adhesion and proliferation, J. Biomed. Mater. Res. - Part A. 102 (2014) 3282–3290. https://doi.org/10.1002/jbm.a.34993.

[37]   M. Heshmati, D. Seifzadeh, P. Shoghi, M. Gholizadeh-Gheshlaghi, Duplex Ni-Zn-Cu-P/Ni-P electroless coating on magnesium alloy via maleic acid pretreatment, Surf. Coatings Technol. 328 (2017) 20–29. https://doi.org/10.1016/j.surfcoat.2017.08.027.

[38]   M. Curioni, The behaviour of magnesium during free corrosion and potentiodynamic polarization investigated by real-time hydrogen measurement and optical imaging, Electrochim. Acta. 120 (2014) 284–292. https://doi.org/10.1016/j.electacta.2013.12.109.

[39]   S. Karamikamkar, A. Abidli, E. Behzadfar, S. Rezaei, H.E. Naguib, C.B. Park, The effect of graphene-nanoplatelets on gelation and structural integrity of a polyvinyltrimethoxysilane-based aerogel, RSC Adv. 9 (2019) 11503–11520. https://doi.org/10.1039/C9RA00994A.

[40] C.J. Brinker, G.C. Frye, A.J. Hurd, C.S. Ashley, Fundamentals of sol-gel dip coating, Thin Solid Films. 201 (1991) 97–108. https://doi.org/10.1016/0040-6090(91)90158-T.

[41] L. Landau, B. Levich, Dragging of a Liquid by a Moving Plate, Acta Physicochim. URSS. 17 (1942) 42–54. https://doi.org/10.1016/b978-0-08-092523-3.50016-2.

[42] H. Du, S.D. Pang, Enhancement of barrier properties of cement mortar with graphene nanoplatelet, Cem. Concr. Res. 76 (2015) 10–19. https://doi.org/10.1016/j.cemconres.2015.05.007.

[43] C. Wu, M. Chen, T. Zheng, X. Yang, Effect of surface roughness on the initial response of MC3T3-E1 cells cultured on polished titanium alloy, Biomed. Mater. Eng. 26 (2015) S155–S164. https://doi.org/10.3233/BME-151301.

[44] H.H. Huang, C. Te Ho, T.H. Lee, T.L. Lee, K.K. Liao, F.L. Chen, Effect of surface roughness of ground titanium on initial cell adhesion, Biomol. Eng. 21 (2004) 93–97. https://doi.org/10.1016/j.bioeng.2004.05.001.

[45] M. Mehrali, E. Moghaddam, S.F.S. Shirazi, S. Baradaran, M. Mehrali, S.T. Latibari, H.S.C. Metselaar, N.A. Kadri, K. Zandi, N.A.A. Osman, Mechanical and in vitro biological performance of graphene nanoplatelets reinforced calcium silicate composite, PLoS One. 9 (2014). https://doi.org/10.1371/journal.pone.0106802.

[46] S.K. Lee, H. Kim, B.S. Shim, Graphene: an emerging material for biological tissue engineering, Carbon Lett. 14 (2013) 63–75. https://doi.org/10.5714/cl.2013.14.2.063.

[47] A.M. Pinto, I.C. Gonçalves, F.D. Magalhães, Graphene-based materials biocompatibility: A review, Colloids Surfaces B Biointerfaces. 111 (2013) 188–202. https://doi.org/10.1016/j.colsurfb.2013.05.022.